



Soft Matter

The effect of external shear flow on the sperm motility

Journal:	<i>Soft Matter</i>
Manuscript ID	SM-ART-04-2019-000717.R1
Article Type:	Paper
Date Submitted by the Author:	11-Jun-2019
Complete List of Authors:	Kumar, Manish; Purdue University System Ardekani, Arezoo; Purdue University System,

SCHOLARONE™
Manuscripts

Cite this: DOI: 10.1039/xxxxxxxxxx

The effect of external shear flow on the sperm motility

Manish Kumar, Arezoo M. Ardekani^a

Received Date

Accepted Date

DOI: 10.1039/xxxxxxxxxx

www.rsc.org/journalname

The trajectory of the sperm in the presence of background flow is of utmost importance for the success of fertilization, as the sperm encounter background flow of different magnitude and direction on their way to the egg. Here, we have studied the effect of an unbounded simple shear flow as well as Poiseuille flow on the sperm trajectory. In the presence of a simple shear flow, the sperm moves on an elliptical trajectory in the reference frame advecting with the local background flow. The length of major-axis of this elliptical trajectory decreases with the shear rate. As the sperm number, a dimensionless number representing the ratio of viscous force to elastic force, increases the flexibility of the flagellum increases, which increases the length of major axis of the elliptical trajectories. The sperm moves downstream or upstream depending on the strength of background flow in the presence of Poiseuille flow. In contrast to the simple shear flow, the sperm also moves toward the centerline in a Poiseuille flow. Far away from the centerline, the cross-stream migration velocity of the sperm increases as the transverse distance of sperm from the centerline decreases. Close to the centerline, on the other hand, the cross-stream migration velocity decreases as the sperm further approaches the center. The cross-stream migration velocity of the sperm also increases with the sperm number.

1 Introduction

For successful fertilization, the human sperm travel a distance 1000 times larger than their length ($\sim 50\mu\text{m}$) through highly flexible tubes of diameter 200 times wider than their own length to reach to the female eggs ($\sim 0.1\text{mm}$), which are 30 times larger than sperm head ($\sim 3-5\mu\text{m}$). Throughout their journey to the egg, the sperm have to navigate by overcoming a complex physiological environment, chemical gradient and counter flow. Due to these complexities, only a small fraction of the initial population is able to reach to the vicinity of human eggs (~ 10 out of hundreds of millions). In the immediate vicinity of the ovum, chemotaxis^{1,2} and thermotaxis³ provide essential guidance to spermatozoa to move toward egg, but far away from the ovum rheotaxis^{4,5} and cervix contraction^{6,7} contribute dominantly in the determination of sperm trajectory. During their journey the fluid through which sperm travels is not static and the sperm encounter flow with different velocities and different directions, even opposite to way the sperm have to swim.

Rheotaxis, through which the sperm is capable of changing its orientation in response to velocity gradient⁸, is a major taxis factor for long distance navigation essential for fertilization^{4,5}. In addition to internal fertilization, the influence of background flow on external fertilization, e.g., marine mollusk have been reported in the literature^{9,10}. The positive rheotaxis of spermatozoa was first reported by Lott¹¹. Bretherton and Rothschild¹² studied the

orientation of sperm in a Poiseuille flow and observed upstream swimming of the motile sperm due to positive rheotaxis in the presence of the Poiseuille flow. The study of mammalian sperm in the Poiseuille flow⁵ have shown that the interplay of fluid shear, steric surface-interaction and chirality of flagellar beat facilitate upstream spiraling motion of sperm along the channel wall for low shear velocity, whereas at a large shear velocity the sperm is simply advected downstream. The theoretical and experimental study of sperm near a solid surface has been done to understand the influence of a time-dependent linear flow gradient on the rheotactic turning of sperm¹³. By considering competition between sperm circling due to asymmetric beating of flagellum and shear induced rotation of sperm, a critical shear rate required for upstream swimming has been derived¹⁴. However, the experimental and theoretical studies on the sperm rheotaxis^{14,15} have shown that the flagellum chirality and surface hydrodynamic interaction are not necessary for rheotaxis and the sperm, even with planar flagellar beating, can swim upstream due to rheotaxis.

Although the sperm rheotaxis in the vicinity of a solid surface have been widely explored^{5,13-16}, the sperm rheotaxis in the bulk fluid still needs to be explored. Rheotaxis does not require surface vicinity and it also occurs in the bulk fluid^{15,17}. The boundary accumulation of sperm does not occur once the distance between surface and flagellum becomes larger than 20% of the flagellum length¹⁵. In this paper, we have studied the effect of unbounded simple shear flow and Poiseuille flow on the sperm motion over a wide range of shear rates by considering sperm with an active flagellum. We model flagellum as an active elastic ele-

^a School of Mechanical Engineering, Purdue University, West Lafayette, Indiana, 47907, USA. E-mail: ardekani@purdue.edu

ment¹⁸ and obtain hydrodynamic forces acting on the flagellum using a Resistive Force Theory (RFT) to avoid flagellum modeling limitations like: small amplitude beating, infinite length and prescribed waveform. RFT gives a good approximation of the hydrodynamic forces on a long cylindrical filament, where hydrodynamic interaction due to finite filament curvature, presence of wall or presence of neighboring filaments are not important^{18–32}. This work provides an insight on the movement of sperm during external^{9,10} as well as internal fertilization⁴. During internal fertilization, the sperm can overcome the wall effect in the oviduct due to hyperactivation^{4,33}. The oviductal fluid flow rate is comparable to the sperm swimming velocity. In mice, oviductal flow rate is in the range $18 \pm 1.6 \mu\text{m/s}$ which is comparable to the sperm swimming velocity $36 - 54 \mu\text{m/s}$ in viscous media⁴. In human, oviductal fluid production rate is $7.92 - 98.4 \text{ml/h}$ ³⁴ and oviduct diameter is $1 \text{mm} - 1 \text{cm}$, leading to an estimation of the oviductal flow rate in the range $28 \mu\text{m/s} - 35 \text{mm/s}$, which is comparable to the swimming velocity of human sperm ($58 - 62 \mu\text{m/s}$)³⁵.

2 Problem statement and governing equations

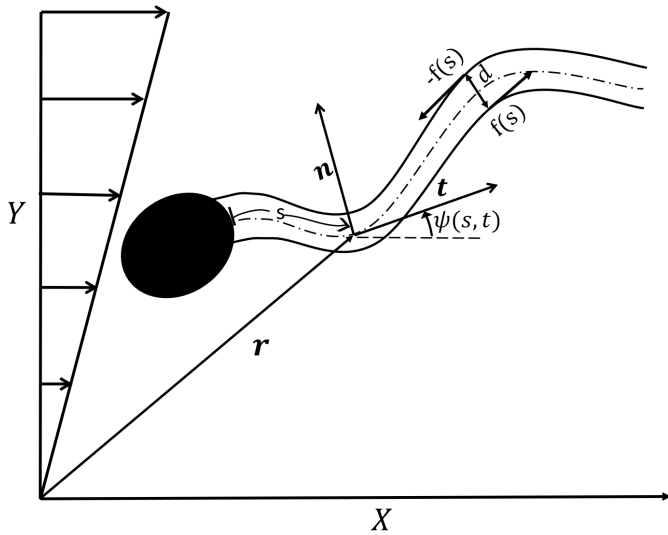


Fig. 1 The schematic of sperm along with ambient flow field. \mathbf{r} represents the position vector for a point on the centerline of the flagellum. X - Y coordinate denotes a fixed frame and s represents the arc-length of flagellum. Shear force field, leading to flagellum beating is shown by $f(s, t)$. Unit vectors \mathbf{t} and \mathbf{n} are tangent and normal vectors to the centerline, respectively. $\psi(s, t)$ is the angle between the tangent vector and the horizontal axis.

Here, we study the motion of sperm in the presence of a planar unbounded simple shear flow and Poiseuille flow using a Resistive Force Theory (RFT). We consider 2-D planar beating of a 3-D cylindrical sperm flagellum, because many experimental studies have reported that the flagellar beating of sperm of many species are approximately planar^{13,24,35,36}. The schematic of the background flow field and the details of the model of an active sperm flagellum have been depicted in figure 1, where a flagellar axoneme of diameter d has been represented by a pair of elastic filaments.

We obtain the governing equations of a flagellum of length L , bending stiffness κ_s and beating frequency ω in the presence of

background flow by balancing the hydrodynamic force with the elastic force per unit length along the arc-length of the flagellum similar to Camalet and Jülicher²⁸ (see figure 1):

$$(\xi_{\parallel} \mathbf{t} \mathbf{t} + \xi_{\perp} \mathbf{n} \mathbf{n}) \cdot \left\{ \frac{\partial \mathbf{r}}{\partial t} - \mathbf{U} \right\} = -\frac{\delta G}{\delta \mathbf{r}}, \quad (1)$$

where \mathbf{U} is the ambient flow field, ξ_{\parallel} and ξ_{\perp} are tangential and normal resistance force coefficients of the flagellum, respectively. The elastic force per unit length on the flagellum has been obtained by taking the spatial derivative of the total elastic energy (G) of the flagellum. The elastic energy of an active sperm flagellum consists of bending energy, extensional energy and active energy²⁸. Therefore, the expression for the elastic energy of flagellum can be given as:

$$G = \int_0^L \left\{ \frac{\kappa_s C^2}{2} + \Lambda \left| \frac{\partial \mathbf{r}}{\partial s} \right|^2 + f \Delta \right\} ds, \quad (2)$$

where C is the local curvature of the flagellum. For an extensible flagellum Λ is the tensile stiffness, whereas it is a Lagrange multiplier for an in-extensible flagellum and ensures local in-extensibility constraint of the flagellum, $\left| \frac{\partial \mathbf{r}}{\partial s} \right|^2 = 1$. The shear force field $f(s, t)$, generated by the dynein motors of flagellar axoneme, creates relative displacement (Δ) between the doublet microtubules^{37–41}, which leads to an additional contribution to the elastic energy.

Here, we consider an in-extensible sperm flagellum and have used length scale L , time scale ω^{-1} , force density scale $\frac{\omega \xi_{\perp} L^2}{d}$ and tension scale $\omega \xi_{\perp} L^2$ to make the governing equations dimensionless. The governing equations of flagellar waveform can be written as:

$$\gamma \ddot{\tau} - (\dot{\psi})^2 \tau + Sp^{-4} \{ (1 + \gamma) \dot{\psi} \dot{\psi} + \gamma \dot{\psi}^2 \} - \{ \gamma f \dot{\psi} + (1 + \gamma) f \dot{\psi} \} + \frac{\partial u_t}{\partial s} = 0, \quad (3)$$

$$\frac{\partial \psi}{\partial t} + Sp^{-4} \{ \ddot{\psi} - \gamma \dot{\psi}^2 \dot{\psi} \} - (1 + \gamma) \dot{\tau} \dot{\psi} - \tau \ddot{\psi} - (f - \gamma \dot{\psi}^2 f) - \frac{\partial u_n}{\partial s} = 0, \quad (4)$$

where $\tau(s, t)$ is the tension profile of the flagellum. The derivatives of τ , ψ and f with respect to the arc-length of the flagellum have been denoted by overdots. $\gamma = \frac{\xi_{\perp}}{\xi_{\parallel}}$ is the ratio of normal to tangential resistive force coefficient and the sperm number $Sp = L \left(\frac{\omega \xi_{\perp}}{\kappa_s} \right)^{\frac{1}{4}}$ represents the relative importance of the viscous drag force to elastic force. The tangential and normal components of the derivative of background flow field (\mathbf{U}) with respect to arc length s are denoted as $\frac{\partial u_t}{\partial s}$ and $\frac{\partial u_n}{\partial s}$, respectively.

The boundary conditions required to solve the governing equations (3 and 4) have been derived using force and torque balance on the flagellar front and distal end. The force and the torque due to the presence of the sperm head balance the force and the torque on the front end of the flagellum ($s = 0$), respectively. The hydrodynamic torque on the sperm head is three orders of magnitude smaller compared to the hydrodynamic torque on the sperm flagellum¹⁵, therefore, the torque due to the presence of the head

can be neglected. The hydrodynamic drag force due to the presence of the sperm head has been approximated by introducing the drag force coefficient ζ ²⁸. The additional drag induced by the sperm head reduces the sperm swimming speed as well as the amplitude of head yawing motion. The dimensionless form of boundary conditions at the front end of the flagellum can be given as:

$$-\zeta\left(\frac{\partial \mathbf{r}}{\partial t} - \mathbf{U}\right) = \mathbf{F}_{head} = (Sp^{-4}\dot{\psi} - f)\mathbf{n} - \tau\mathbf{t}, \quad (5)$$

$$0 = T_{head} = -Sp^{-4}\dot{\psi} - \int_0^1 f ds. \quad (6)$$

The distal end of the sperm flagellum has been considered force and torque free, which leads to the following dimensionless boundary conditions at the flagellum distal end, $s = 1$:

$$0 = (-Sp^{-4}\ddot{\psi} + f)\mathbf{n} + \tau\mathbf{t}, \quad (7)$$

$$0 = Sp^{-4}\dot{\psi}. \quad (8)$$

The shear force field, $f(s, t)$, is the driving force of the flagellar beating and the input of the present model of the sperm flagellum. The model based on the internal shear force field has successfully explained the flagellar beating of the sperm^{18,24,26–28,31}, however there is limited quantitative understanding of its form. Here, we obtain the internal shear force by solving the governing equations (3 and 4) for shear force $f(s, t)$ (instead of $\psi(s, t)$) that generates a given beating pattern in a quiescent fluid ($\psi_0(s, t)$). We use the following model of sperm flagellar waveform in a quiescent fluid which provides a good representative of mammalian sperm beating pattern in a fluid with comparable viscosity to cervical mucus^{35,42} (see supplementary video 1):

$$\psi_0(s, t) = s \cos(2\pi s - t). \quad (9)$$

The governing equations of the flagellar dynamics (3 and 4) are highly nonlinear and coupled. We use a semi-implicit method to solve equation (4), where only the highest order derivative of each nonlinear term is discretized implicitly (t_{n+1}) and the rest are considered at previous time step (t_n). The tension profile $\tau(s, t)$ at time step t_n is required to solve equation (4). τ_n has been obtained by solving equation (3) using ψ_n , the waveform at time step t_n . The spatial discretization is uniform along the arc length of the flagellum and the spatial derivatives at each grid point are approximated with five closest grid values. Even though, the numerical scheme is stable even at larger time steps, we have used $\Delta t \sim (Sp \cdot \Delta s)^4$ to maintain the accuracy of the results. The time advancement of sperm has been obtained by evaluating equation 1 at $s = 0$, (i.e., $\mathbf{r}(0, t)$). The flagellar shape is then constructed from the local tangent angle $\psi(s, t)$ as $\mathbf{r}(s, t) = \mathbf{r}(0, t) + \int_0^s (\cos(\psi), \sin(\psi)) ds'$.

We validate our numerical code against the numerical and experimental results of an elastic filament actuated at its end^{20–22}. To replicate the formulation of an end actuated elastic filament, we assume a zero internal shear force $f = 0$ and head position $s = 0$ subject to a periodic actuation. The propulsive force calculated by the present nonlinear numerical scheme provides a

good agreement with the propulsive force obtained by Yu *et al.*²² (see Appendix). To be consistent with Wiggins and Goldstein²⁰, we also linearize the equations for small deflection and find that the propulsive force prediction of linear and nonlinear numerical schemes match very well with published results of Wiggins and Goldstein²⁰. Furthermore, we validate the implementation of the internal shear force against the analytical study of Camalet and Jülicher²⁸, where the leading order term of the sperm swimming speed is reported to be proportional to the square of the amplitude of the shear force (see Appendix for more details).

3 Results and Discussion

The sperm number, $Sp = L\left(\frac{\omega\xi_{\perp}}{\kappa_s}\right)^{\frac{1}{4}}$, representing the ratio of hydrodynamic force to elastic force, takes a wide range of values as flagellum size, flagellum mechanical properties and the viscosity of medium through which sperm swim vary a lot among the species. The resistive force coefficient ξ_{\perp} varies from $1.4 \times 10^{-3} \text{Ns/m}^2$ for low viscosity watery medium to 3.2Ns/m^2 for highly viscous in vitro fertilization medium³⁵. Human sperm have length $L = 36 - 50 \mu\text{m}$ ⁴³, bending stiffness $\kappa_s = 4 \times 10^{-21} \text{Nm}^2$ ⁴⁴ and beating frequency $\omega = 11 - 24 \text{Hz}$ ³⁵, therefore sperm number is in the range of $Sp = 1.6 - 19$. The bending stiffness of sea urchin sperm $\kappa_s = 0.9 \times 10^{-21} \text{Nm}^2$ ⁴⁵, length $L = 30 - 45 \mu\text{m}$ and beating frequency $\omega = 25 - 40 \text{Hz}$ ³⁶ lead to $Sp = 2.3 - 4$ in water. *Caenorhabditis elegans*, an undulatory nematode of length 1mm , bending stiffness $\kappa_s = 2.6 \times 10^{-15} \text{Nm}^2$ and beating frequency $\omega = 1.7 \text{Hz}$ have sperm number $Sp = 1.0$ in water⁴⁶. In the present study, we are not considering very large sperm numbers, so that the sperm flagellum does not buckle and beating pattern remains symmetric. By reverse calculation, we obtain the shear force field at $Sp = 1.0$ in the presence of a quiescent fluid and use it to study the effect of Sp and shear strength on the sperm trajectory.

At small sperm numbers, the sperm flagellum doesn't buckle. Therefore, the beating of sperm flagellum remains symmetric and the net motion of sperm is along a straight line in a quiescent fluid with a yawing head trajectory (supplementary video 1). Here, we study the swimming motion of sperm in a simple shear flow as well as Poiseuille flow. The sperm rotates clockwise for positive shear and counter-clockwise for negative shear along with a yawing motion of head.

3.1 The sperm navigation in a simple shear flow

Dimensionless simple shear flow velocity U_s has been defined as $U_s = \dot{\gamma}L/u_{sperm}$, where $\dot{\gamma}$ and u_{sperm} are shear rate and sperm average swimming speed at $Sp = 1.0$ in the quiescent fluid, respectively.

The trajectories of sperm head, which is averaged over a flagellar beating period, in a simple shear flow at different initial locations have been shown in figure 2. In the simple shear flow, the sperm moves downstream by making a periodic trajectory without net cross-stream migration (figure 2b and 2c). The trajectories at different positions in the flow are related by a superimposed translation due to the translational invariance of simple shear flow in the gradient direction. The local flow velocity increases as the distance of sperm from the centerline of the flow

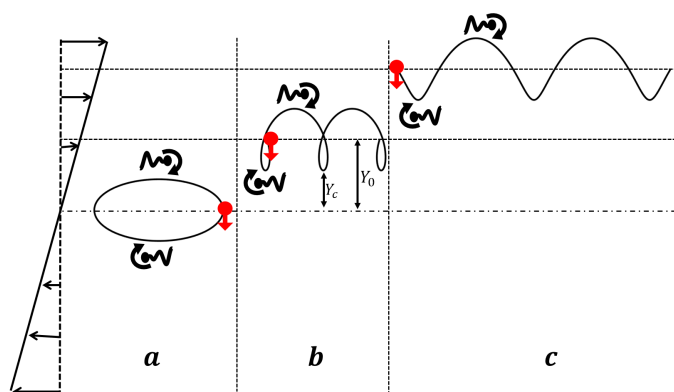
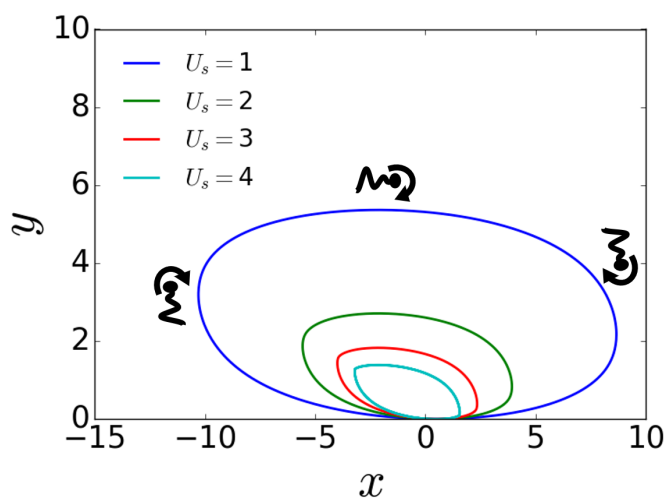


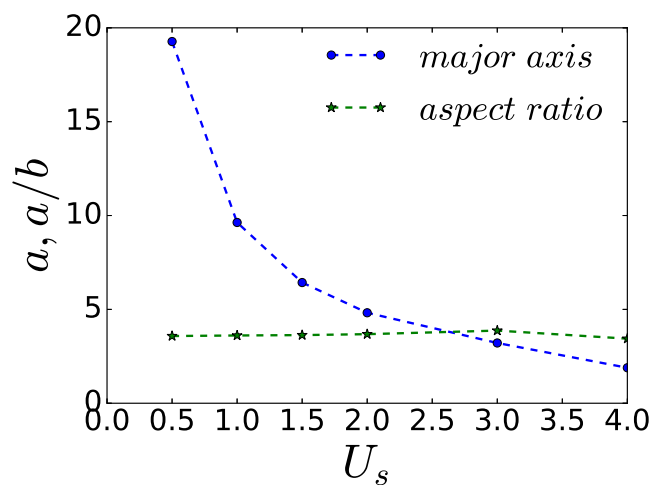
Fig. 2 The schematic of sperm head trajectory in a simple shear flow. Solid line represents average trajectory of sperm head. Solid circles and arrows indicate initial location and initial orientation of the sperm, respectively. The small sketches of sperm along the trajectory line represent the orientation of sperm and the cyclic arrows at the head of sperm represent the direction of sperm rotation at that location.

increases. Therefore, close to the centerline the sperm swims upstream when its orientation is opposite to the flow direction (figure 2b), whereas far away from the centerline the local flow dominates over the sperm's swimming velocity and the sperm gets advected downstream irrespective of its orientation (figure 2c). The transition of sperm trajectory from figure 2b to figure 2c takes place once the characteristic distance (Y_c) of sperm satisfies condition: $U_s Y_c > 1$, where Y_c is the distance of sperm from the centerline of the flow when it points in the opposite direction of the flow (see figure 2). The definition of Y_c also implies that Y_c is the minimum distance of the sperm during a full rotation from the centerline in a simple shear flow (figure 2) whereas it is the maximum distance in a Poiseuille flow (see figure 5). The net displacement of sperm during full-rotation decreases as the sperm gets closer to the centerline of shear flow and eventually it gets trapped at $Y_0 = 0$ (figure 2a). Y_0 is the average transverse distance of the sperm from the centerline (see figure 2). In this case, the sperm crosses the centerline and the net displacement is zero during full-rotation. The rheotactic behavior of flagellated bacteria in a simple shear flow has been observed both experimentally¹⁷ and theoretically⁴⁷.

Although the sperm follows multiple trajectories depending on its initial location and orientation in the simple shear flow, it makes a unique elliptical trajectory independent to the initial location and orientation in the reference frame advecting with the background flow at Y_0 due to translational invariance of shear rate (figure 3a). The velocities and trajectories reported hereafter in this sub-section are reported in the reference frame advecting with the background flow at Y_0 . The angular velocity of the sperm during its rotation depends on the shear rate as well as sperm orientation. The angular velocity of sperm increases as the shear rate increases and for a given shear rate the angular velocity is maximum when the sperm orients perpendicular to the streamlines (see supplementary video 2). This leads to an elliptical shape of sperm trajectory with a decreasing size as the shear rate increases (figure 3a). Although, the length of major axis of elliptical trajectory decreases as the shear rate increases, the as-



(a)

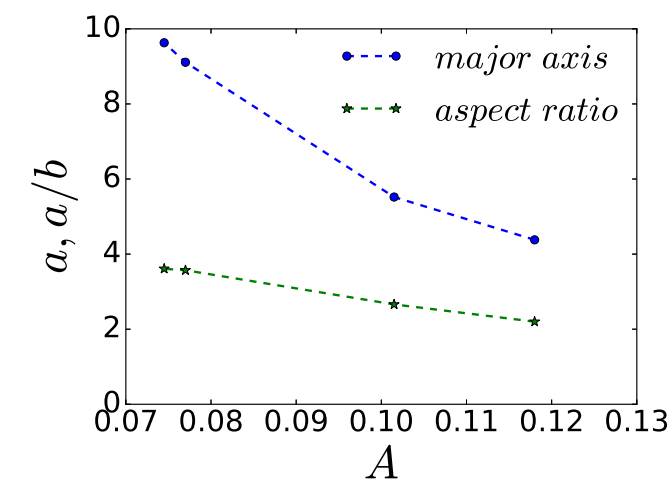


(b)

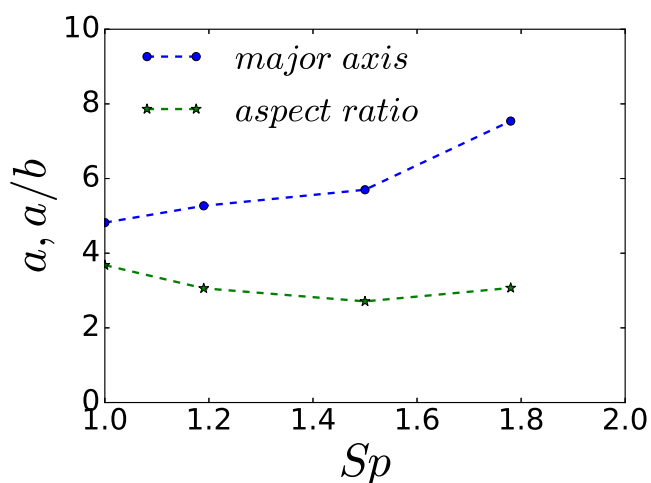
Fig. 3 (a) Swimming trajectory of sperm in the reference frame advecting with the background flow at Y_0 for different shear rates. (b) Major axis (a) and aspect ratio (a/b) of elliptical trajectory of sperm at different shear rates.

pect ratio (a/b) of ellipse remains nearly invariant (figure 3b). To quantify the size of the elliptical trajectory, we calculate eigen values (λ_1, λ_2) of the matrix representing the second moment of area: $I_{ij} = \int (x_i - x_i^c)(x_j - x_j^c)dA$, where $x_i^c = \frac{1}{A} \int x_i dA$ is the centroid of the ellipse. The aspect ratio (a/b) of the trajectory can be given as, $a/b = \sqrt{(\lambda_1/\lambda_2)}$ and length of major axis (a) can be estimated by using aspect ratio and the area of ellipse.

The amplitude of the yawing motion of sperm's head also influences the trajectory of the sperm. If the sperm orients parallel (perpendicular) to the streamlines of the flow, the angular velocity of the sperm increases (decreases) as the amplitude of the yawing motion of sperm increases. This leads to a smaller aspect ratio as well as smaller major-axis of the elliptical trajectory for the sperm having larger head yawing amplitude (figure 4a). The presence of sperm head induces elliptical trajectory with larger aspect ratio as the presence of head reduces the yawing amplitude of the sperm motion.



(a)



(b)

Fig. 4 (a) Major axis (a) and the aspect ratio (a/b) of sperm's trajectory at different head yawing amplitude (A) for ambient flow velocity $U_s = 1$. (b) Major axis (a) and the aspect ratio (a/b) of sperm's trajectory at different Sp for ambient flow velocity $U_s = 2$.

The shear force field of sperm is generated by the dynein motors of flagellar axoneme, whereas Sp can be changed even through changing the viscosity of the medium. Therefore, it is reasonable for a given sperm to assume a fixed shear force field with varying Sp as the sperm changes its swimming medium. For a given flagellum shear force field $f(s,t)$, the beating pattern of the flagellum changes with the sperm number. We have calculated the shear force field at $Sp = 1.0$ and have used it to study the effect of Sp on the sperm trajectory. The effective viscosity of the cervical mucus varies from $0.2 Pa \cdot s$ in day 0 of menstrual cycle to $0.68 Pa \cdot s$ in day 5 of menstrual cycle³⁵, changing the mucus viscosity by 3 times. For a given $f(s,t)$ of a particular sperm we consider the range of $Sp = 1.0 - 1.78$, which corresponds to 10 times change in the viscosity of the medium. The length of major-axis of the ellipse increases as Sp increases (figure 4b), because the flexibility of the flagellum increases as the sperm number in-

creases and the net swimming velocity of sperm in the quiescent fluid also increases with increasing flexibility of the flagellum for a given $f(s,t)$ (see Appendix). The flexibility of flagellum reduces the difference between the angular velocity of sperm parallel and perpendicular to the streamlines. Therefore, the aspect ratio of the ellipse decrease as the flexibility of flagellum increases.

3.2 The sperm navigation in a Poiseuille flow

The sperm exhibits a more complex trajectory in the presence of Poiseuille flow compared to a simple shear flow, because neither shear strength nor shear direction is constant throughout the domain in the Poiseuille flow. Rescaled magnitude of the Poiseuille flow has been defined as $U_s = (u_{max}/u_{sperm})\frac{1}{H}$, where u_{max} is the flow velocity at the centerline of the channel and $2H$ is the dimensionless width of the channel of a Poiseuille flow. We have used $H = 10$ in the present study.

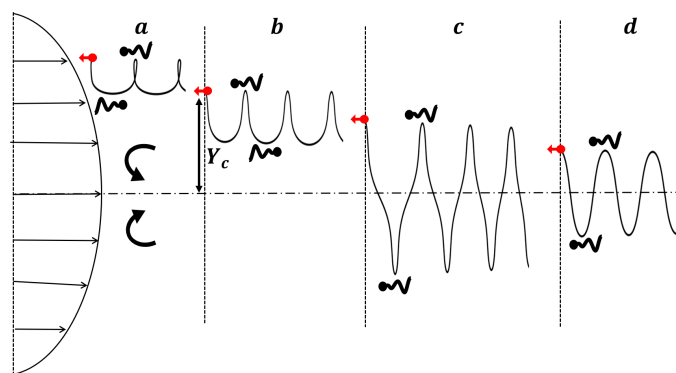


Fig. 5 The trajectory of sperm head in an unbounded Poiseuille flow. Red solid circles and arrows represent initial location and initial orientation of the sperm. Cyclic arrows represent the direction of sperm rotation and small schematics of sperm denote the orientation of the sperm at specified locations. Vertical dotted line separate the zones of dissimilar trajectories from each-other. (a) The trajectory of sperm head is close to the wall, where shear rate is the highest, but flow velocity is minimum. (b) and (c) The trajectory of sperm head is in between wall and the centerline of the flow. In (b), sperm doesn't cross the centerline of the flow. In (c), sperm crosses the centerline of the flow. (d) The trajectory of sperm head is close to the centerline of the flow.

The trajectory of the sperm head, which is averaged over flagellar beating period, at various locations across the cross-section of the channel has been depicted in figure 5. The direction of rotation of sperm changes from counter-clockwise in the upper half of the channel to clockwise in the bottom half of the channel as the sign of shear rate changes from negative in the upper half to positive in the bottom half of the channel. In the Poiseuille flow, the sperm travels either upstream or downstream depending on the strength of the flow. The trajectory of sperm in the Poiseuille flow can be divided into four distinct regimes (see figure 5). Far away from the centerline of the flow, if the shear strength is not too weak, the sperm makes full rotation and is not able to cross the centerline of flow (figure 5a and 5b). This type of tumbling motion has also been observed for non-flagellated spherical and elongated micro-swimmers in a Poiseuille flow away from the centerline^{48,49}. Close to the wall, the swimming speed of sperm dominates over the background flow. This leads to up-

stream swimming of the sperm when it orients against the flow direction, however the sperm net motion is in the downstream direction (figure 5a). The sperm travels downstream regardless of its orientation, if it doesn't cross the centerline and the sperm swimming speed is less than the background flow, (figure 5b). The value of Y_c required for the transition between figure 5a to figure 5b is $1 < U_s H [1 - (Y_c/H)^2]$. Close to the centerline, the sperm crosses the centerline and swings without making a complete rotation (figure 5c and 5d). Y_c , for which the sperm aligns with the streamlines at the centerline, is the value of Y_c required for the transition between figure 5b to figure 5c. Thus, the span of rotation decreases monotonically from 180° for the trajectory just after the transition (figure 5c) to 0° (figure 5d) as the sperm reaches the centerline at a larger time in case of trajectories without any inflection point. Due to small amplitude of swinging rotation at very large time, the sperm keeps pointing upstream (figure 5d). This leads to net upstream swimming of the sperm in figure 5d if the sperm swimming velocity is larger than the local ambient flow velocity (i.e., $U_s H < 1$), otherwise the sperm gets advected downstream even in figure 5d. Net upstream swimming has been also reported in the literature for non-flagellated micro-swimmers and helical flagellated bacteria, when they are close to the centerline of Poiseuille flow^{47–49}. Moreover, the positive rheotaxis of mammalian sperm has been confirmed by both in situ and in vitro experiments^{4,5}. Here we show that the interplay of flagellar flexibility and decreasing shear rate near the centerline leads to a net drift of sperm toward the centerline of a Poiseuille flow. A net drift toward the centerline of Poiseuille flow has also been observed for bacteria with a helical flagellum⁴⁷, whereas non-flagellated rigid micro-swimmers do not exhibit net cross-stream migration toward the centerline^{48,49}. The net drift toward the centerline of Poiseuille flow due to the elastic flagellum allows sperm to switch from tumbling motion (figure 5a and 5b) to swinging motion (figure 5c and 5d) as the sperm crosses the centerline of the flow. Non-flagellated micro-swimmers also exhibit tumbling and swinging behavior depending on their initial position, but the transition from tumbling to swinging is not feasible^{48,49}. The value of Y_c required to cross the centerline (i.e. switch from tumbling to swinging motion) increases as the strength of flow decreases. Therefore for a weak background flow, the value of Y_c for the transition from figure 5b to figure 5c becomes very large and the sperm mainly exhibits trajectories like 5d.

Next, we quantify the net migration velocity of the sperm in the Poiseuille flow, which is defined as the displacement of sperm head during one cycle of sperm periodic motion. The plots, representing the cross-stream migration of sperm (figure 6a,6b, 7a and 7b), have been created using different runs with different starting distances from the centerline (h). For all the runs, the initial orientation of sperm is against the flow direction. Figure 6a represents the cross-stream migration velocity (v) toward the centerline of the Poiseuille flow at different distances (h) from the centerline. The cross-stream migration velocity of sperm increases as the shear rate increases for swinging motion (the sperm crosses the centerline of the Poiseuille flow), while decreases for tumbling motion (the sperm makes full rotation and doesn't cross

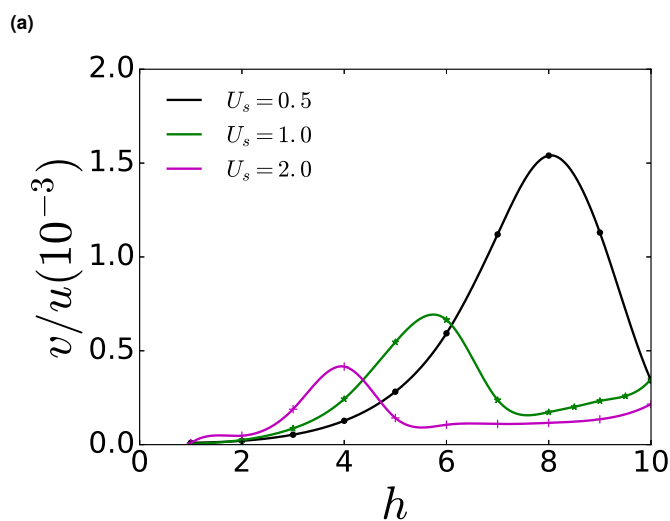
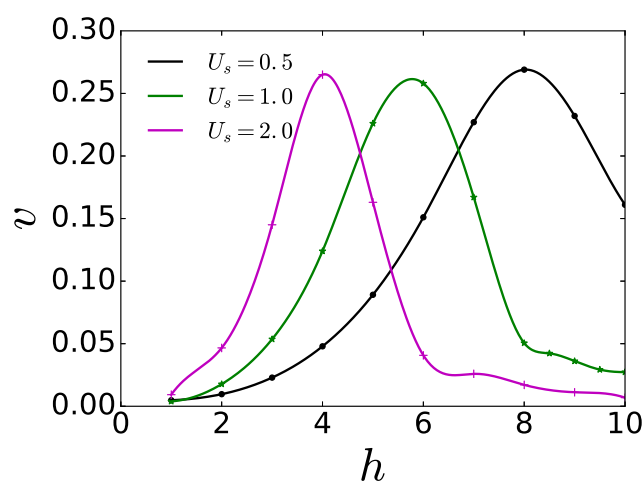


Fig. 6 (a) Cross-stream migration velocity (v) vs transverse distance of sperm from the centerline of the Poiseuille flow (h) at different background flow velocities. (b) The ratio of cross-migration to downstream migration (v/u) of the sperm vs distance of sperm from the centerline of the Poiseuille flow at different background flow velocities.

the centerline of the flow). Initially, far away from the centerline, the cross-stream migration velocity of sperm increases as the sperm approaches the centerline, because the sperm doesn't cross the centerline and shear rate decreases toward the center of the flow. After some time, the sperm starts crossing the centerline of the flow and the cross-stream migration velocity of sperm starts decreasing as the sperm further approaches the centerline (figure 6a). As the strength of background flow increases, the value of Y_c required to cross the centerline of the flow decreases. Therefore, the transverse distance of sperm from the centerline, at the instance of maximum cross-migration velocity, decreases as the strength of background flow increases (figure 6a). The maximum cross-stream migration velocity of the sperm is nearly independent of the strength of background flow. Figure 6b depicts the ratio of cross-migration to downstream migration at different transverse location of the sperm. The maximum value of

the ratio of cross-stream migration to downstream-migration decreases as the background flow velocity increases.

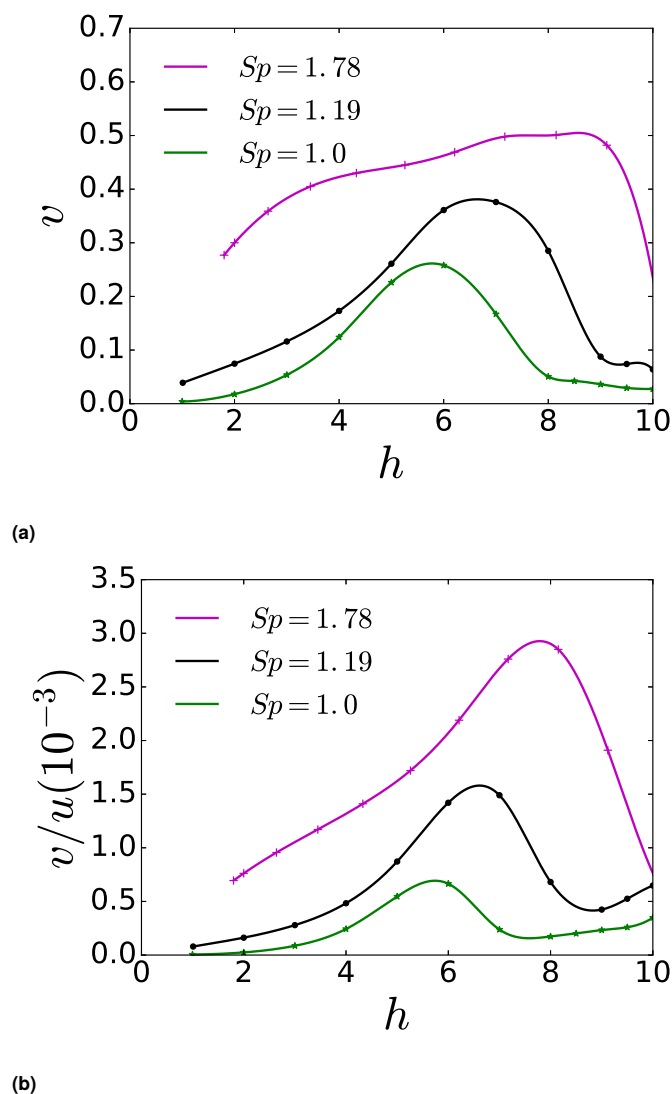


Fig. 7 (a) Cross-stream migration velocity vs the transverse distance of sperm from the centerline of the Poiseuille flow (h) at different Sp . (b) The ratio of cross-stream migration to downstream migration of the sperm vs distance of sperm from the centerline of the Poiseuille flow at different Sp .

Figure 7a depicts the cross-stream migration velocity of the sperm at different sperm numbers of the flagellum. The flexibility of the sperm flagellum increases as Sp increases and the swimming velocity of sperm increases with flagellar flexibility (Appendix). Therefore, the cross-migration velocity of the sperm increases as Sp increases. The transverse distance of the sperm from the centerline, at the instance of maximum cross-stream migration velocity, increases as Sp increases. Because, the value of Y_c required to cross the centerline increases with Sp due to larger orbits. The ratio of cross-stream migration to downstream-migration has been depicted in figure 7b. Although the qualitative behaviours of graphs are independent of Sp , it increases as Sp increases (figure 7b).

4 Conclusions

We have studied the effect of planar unbounded simple shear flow and Poiseuille flow on the sperm motility at different shear rates. We have also studied the effect of fluid viscosity and flagellum stiffness on the trajectory of sperm using the sperm number (Sp). Rheotaxis leads to sperm rotation in the clockwise direction in the presence of positive shear and counter-clockwise in the presence of negative shear. The sperm moves downstream in a simple shear flow on periodic trajectories of constant transverse amplitude. In the reference frame advecting with the background flow at Y_0 , the sperm moves on a closed elliptical trajectory, the size of which decreases as the shear strength increases. In contrast to a simple shear flow, the sperm moves downstream or upstream depending on the shear strength in a Poiseuille flow by making periodic trajectories of different transverse amplitude. In a simple shear flow the sperm does not have net cross-stream migration, while in the presence of Poiseuille flow the sperm has a net motion toward the centerline. Far away from the center of the Poiseuille flow, the cross-stream migration velocity of the sperm increases as the transverse distance of sperm from the centerline decreases. But close to the centerline, the cross-stream migration velocity decreases as the sperm further approaches to the center. The flexibility of flagellum increases as the sperm number increases and this leads to a larger ellipse in the simple shear flow and larger cross-stream migration velocity in the Poiseuille flow. The non-flagellated micro-swimmers also exhibit periodic motion similar to flagellated micro-swimmers in a shear flow^{48,49}. However, the cross-stream drift of swimmers has been observed only for elastic flagellated micro-swimmers. The tumbling motion and smaller orbits at high shear rates lead to temporary trapping of micro-swimmers in high shear regions, which is the possible explanation of cell depletion observed in the low shear regions during microfluidic experiments⁵⁰. Although we obtain $f(s, t)$ at $Sp = 1.0$ in the present study, the characteristics of the sperm trajectories are independent of Sp as long as the flagellar beating is symmetric. The method used in the present study to obtain $f(s, t)$ for the mammalian sperm can be easily extended to the sperm of other species (supplementary video 3). The present results can be useful for the design of microfluidic devices for sperm sorting and analysis.

5 Appendix

5.1 Validation of numerical tool

We validated our numerical code against the study of an elastic filament actuated at its end^{20–22}. We assumed force field $f(s, t) = 0$ (equation 3 and equation 4) and head position $s = 0$ is subject to an angular periodic actuation, $\psi(0, t) = \theta_0 \cos(t)$. This leads to following boundary conditions at $s = 0$:

$$\psi(0, t) = \theta_0 \cos(t), \quad (10)$$

$$0 = (-Sp^{-4}\ddot{\psi} + \tau\dot{\psi})\mathbf{n} + \gamma(Sp^{-4}\dot{\psi}\dot{\psi} + \dot{\tau})\mathbf{t}. \quad (11)$$

The distal end of the flagellum ($s = 1$) was assumed to be force and torque free:

$$0 = (-Sp^{-4}\ddot{\psi})\mathbf{n} + \tau\mathbf{t}, \quad (12)$$

$$0 = Sp^{-4}\dot{\psi}. \quad (13)$$

The dimensionless propulsive force F imparted to the fluid by the filament can be written as: $F = \{\dot{\psi} \sin(\psi) - \frac{1}{2}(\dot{\psi})^2 \cos(\psi)\}|_{s=0}$.

We also linearized the governing equation for small deformations:

$$\frac{\partial y}{\partial t} = -Sp^{-4} \frac{\partial^4 y}{\partial x^4}. \quad (14)$$

The boundary conditions at the front end ($x = 0$) of the filament are given as: $y = 0$, $\frac{\partial y}{\partial x} = \theta_0 \cos(t)$ and at the distal end of the filament ($x = 1$) are given as: $\frac{\partial^2 y}{\partial x^2} = 0$, $\frac{\partial^3 y}{\partial x^3} = 0$.

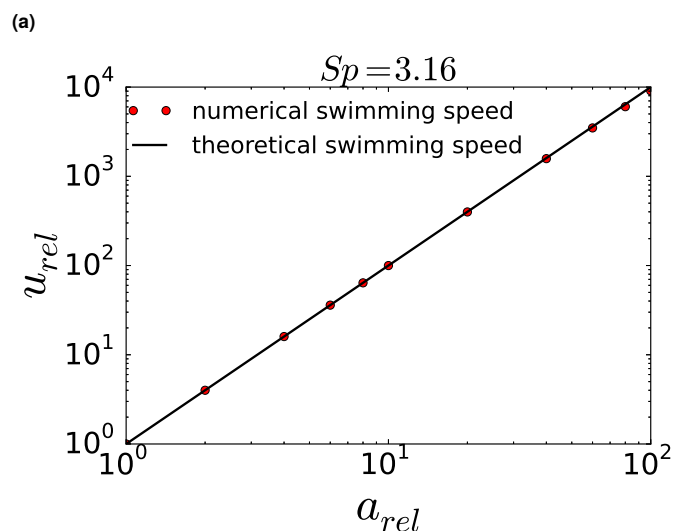
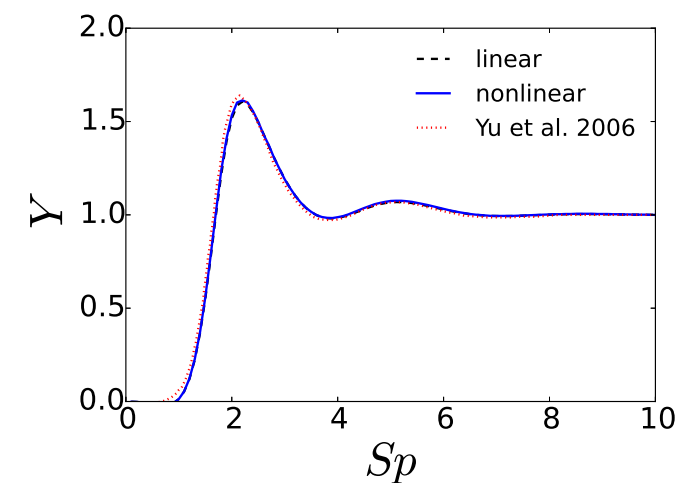


Fig. 8 (a) The scaling function of the propulsive force $Y(Sp)$ at different Sp for the end actuated elastic filament. (b) Relative swimming speed of the sperm at different amplitude of shear force field. u_{rel} and a_{rel} are relative swimming speed and relative amplitude of $f(s, t)$, respectively.

For a small curvature, the propulsive force imparted to the fluid can be approximated as: $F = \{\frac{\partial^3 y}{\partial x^3} \frac{\partial y}{\partial x} - \frac{1}{2}(\frac{\partial^2 y}{\partial x^2})^2\}|_{x=0}$. The time

average of propulsive force (\bar{F}) over one period gives:

$$\bar{F} = \frac{1}{2}\theta_0^2 Sp^2 Y(Sp), \quad (15)$$

where $Y(Sp)$ is the scaling function of the propulsive force. The trend of $Y(Sp)$ vs Sp , obtained from linear as well as non-linear numerical schemes, have been plotted against the result of Yu *et al.*²² in figure 8a. Our result also provides excellent agreement with the prediction of Wiggins and Goldstein²⁰. To validate the implementation of $f(s, t)$, we calculated the average swimming speed of sperm at different amplitude (a) of $f(s, t)$ by assuming a periodic shear force field: $f(s, t) = a \cos(2\pi s - t)$. The swimming speed of sperm obtained from the simulation is plotted against the theoretical prediction of Camalet and Jülicher²⁸ in figure 8b.

5.2 Sperm swimming velocity in the quiescent fluid

For a given $f(s, t)$, the swimming velocity of sperm increases as the flexibility of flagellum increases (figure 9).

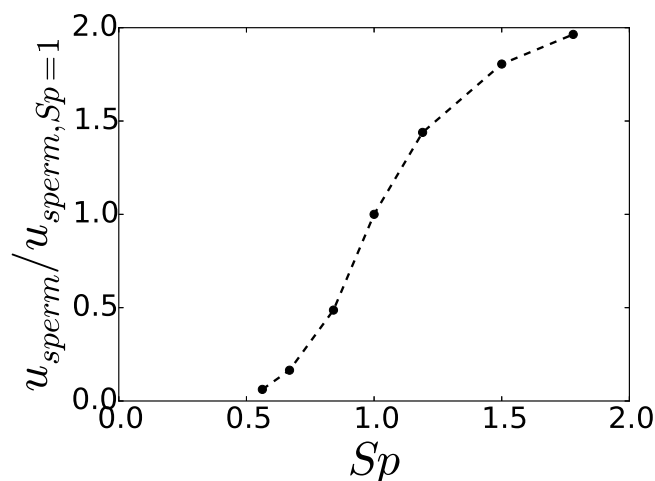


Fig. 9 Net swimming velocity of sperm at different Sp for a given $f(s, t)$. Force field $f(s, t)$ has been obtained at $Sp = 1.0$.

6 Conflicts of interest

There are no conflicts of interest to declare.

7 Acknowledgement

This work is supported by NSF, Grants No. CBET- 1700961.

References

- 1 U. B. Kaupp, N. D. Kashikar and I. Weyand, *Annual Review of Physiology*, 2008, **70**, 93–117.
- 2 M. Spehr, G. Gisselmann, A. Poplawski, J. A. Riffell, C. H. Wetzel, R. K. Zimmer and H. Hatt, *Science*, 2003, **299**, 2054–2058.
- 3 A. Bahat, I. Tur-Kaspa, A. Gakamsky, L. C. Giojalas, H. Breitbart and M. Eisenbach, *Nature Medicine*, 2003, **9**, 149–150.
- 4 K. Miki and D. E. Clapham, *Current Biology*, 2013, **23**, 443–452.

- 5 V. Kantsler, J. Dunkel, M. Blayney and R. E. Goldstein, *eLife*, 2014, **3**, 1–12.
- 6 L. J. Fauti and R. Dillon, *Annual Review of Fluid Mechanics*, 2006, **38**, 371–394.
- 7 D. F. Katz, E. Z. Drobnis and J. W. Overstreet, *Gamete Research*, 1989, **22**, 443–469.
- 8 A. M. Roberts, *Nature*, 1970, **228**, 375–376.
- 9 R. K. Zimmer and J. A. Riffell, *Proceedings of the National Academy of Sciences*, 2011, **108**, 13200–13205.
- 10 J. A. Riffell and R. K. Zimmer, *Journal of Experimental Biology*, 2007, **210**, 3644–3660.
- 11 G. Lott, *Zur Anatomie und Physiologie des Cervix uteri*, Enke, 1872.
- 12 F. P. Bretherton and Rothschild, *Proceedings of the Royal Society B: Biological Sciences*, 1961, **153**, 490–502.
- 13 A. Bukatin, I. Kukhtevich, N. Stoop, J. Dunkel and V. Kantsler, *Proceedings of the National Academy of Sciences*, 2015, **112**, 15904–15909.
- 14 C. K. Tung, F. Ardon, A. Roy, D. L. Koch, S. S. Suarez and M. Wu, *Physical Review Letters*, 2015, **114**, 1–5.
- 15 K. Ishimoto and E. A. Gaffney, *Journal of The Royal Society Interface*, 2015, **12**, 20150172–20150172.
- 16 T. Omori and T. Ishikawa, *Physical Review E*, 2016, **93**, 032402.
- 17 Marcos, H. C. Fu, T. R. Powers and R. Stocker, *Proceedings of the National Academy of Sciences*, 2012, **109**, 4780–4785.
- 18 K. E. Machin, *The Journal of experimental biology*, 1958, **35**, 796–806.
- 19 R. E. Goldstein and S. A. Langer, *Physical Review Letters*, 1995, **75**, 1094–1097.
- 20 C. H. Wiggins and R. E. Goldstein, *Physical Review Letters*, 1998, **80**, 3879–3882.
- 21 C. H. Wiggins, D. Riveline, A. Ott and R. E. Goldstein, *Biophysical Journal*, 1998, **74**, 1043–1060.
- 22 T. S. Yu, E. Lauga and A. E. Hosoi, *Physics of Fluids*, 2006, **18**, 1–5.
- 23 L. Bourdieu, T. Duke, M. B. Elowitz, D. A. Winkelmann, S. Leibler and A. Libchaber, *Physical Review Letters*, 1995, **75**, 176–179.
- 24 I. H. Riedel-Kruse and A. Hilfinger, *HFSP Journal*, 2007.
- 25 C. J. Brokaw, *The Journal of experimental biology*, 1965, **43**, 155–169.
- 26 C. J. Brokaw, *The Journal of experimental biology*, 1971, **55**, 289–304.
- 27 S. Camalet, F. Jülicher and J. Prost, *Physical Review Letters*, 1999, **82**, 1590–1593.
- 28 S. Camalet and F. Jülicher, *New Journal of Physics*, 2000, **2**, 24–24.
- 29 H. C. Fu, C. W. Wolgemuth and T. R. Powers, *Physical Review E - Statistical, Nonlinear, and Soft Matter Physics*, 2008, **78**, 1–12.
- 30 A. Hilfinger, A. K. Chattopadhyay and F. Jülicher, *Physical Review E*, 2009, **79**, 051918.
- 31 M. Hines and J. J. Blum, *Biophysical Journal*, 1978, **23**, 41–57.
- 32 A. Hilfinger and F. Jülicher, *Physical Biology*, 2008, **5**, year.
- 33 S. S. Suarez and A. A. Pacey, *Human Reproduction Update*, 2006, **12**, 23–37.
- 34 J. I. Tay, A. J. Rutherford, S. R. Killick, S. D. Maguiness, R. J. Partridge and H. J. Leese, *Human Reproduction*, 1997, **12**, 2451–2456.
- 35 D. J. Smith, E. A. Gaffney, H. Gadelha, N. Kapur and J. C. Kirkman-Brown, *Cell Motility and the Cytoskeleton*, 2009, **66**, 220–236.
- 36 J. Gray and G. J. Hancock, *Journal of Experimental Biology*, 1955, **32**, 802–814.
- 37 C. Brokaw, *Science*, 1989, **243**, 1593–1596.
- 38 K. E. Summers and I. R. Gibbons, *Proceedings of the National Academy of Science*, 1971, **68**, 3092–3096.
- 39 I. R. Gibbons and A. J. Rowe, *Science*, 1965, **149**, 424–426.
- 40 M. E. Porter and W. S. Sale, *Journal of Cell Biology*, 2000, **151**, 37–42.
- 41 G. G. Vernon and D. M. Woolley, *Cell Motility and the Cytoskeleton*, 2002, **52**, 151–160.
- 42 T. D. Montenegro-Johnson, D. J. Smith and D. Loghin, *Physics of Fluids*, 2013, **25**, year.
- 43 J. A. Mossman, J. T. Pearson, H. D. Moore and A. A. Pacey, *Human Reproduction*, 2013, **28**, 22–32.
- 44 H. Gadêlha, E. A. Gaffney, D. J. Smith, J. C. Kirkman-Brown, H. Gade, E. A. Gaffney and D. J. Smith, *Journal of the Royal Society Interface*, 2010, **7**, 1689–1697.
- 45 M. Okuno, *The Journal of Cell Biology*, 1980, **85**, 712–725.
- 46 J. Sznitman, X. Shen, P. K. Purohit and P. E. Arratia, *Experimental Mechanics*, 2010, **50**, 1303–1311.
- 47 M. Tournus, A. Kirshtein, L. V. Berlyand and I. S. Aranson, *Journal of The Royal Society Interface*, 2014, **12**, 20140904–20140904.
- 48 A. Zöttl and H. Stark, *Physical Review Letters*, 2012, **108**, 218104.
- 49 A. Zöttl and H. Stark, *European Physical Journal E*, 2013, **36**, year.
- 50 R. Rusconi, J. S. Guasto and R. Stocker, *Nature Physics*, 2014, **10**, 212–217.